Supplemental Materials

Multiple Biotic Interactions Establish Phytoplankton Community Structure Across Environmental Gradients

Stephanie Dutkiewicz[1,2], Christopher L. Follett[3,1], Michael J. Follows[2], Fernanda Henderikx-Freitas[4], Francois Ribalet[5], Mary R. Gradoville[6], Sacha N. Coesel[5], Hanna Farnelid[7], Zoe V. Finkel[8], Andrew J. Irwin[9], Oliver Jahn[1], David M. Karl[4,10], Jann Paul Mattern[11], Angelicque E. White[4,10], Jon Zehr[11], E. Virginia Armbrust[5]

1.Department of Earth Atmosphere and Planetary Sciences, Massachusetts Institute of Technology, Cambridge, MA, USA
2.Center for Global Change Sciences, Massachusetts Institute of Technology, Cambridge MA, USA
3.Department of Earth, Ocean and Ecological Sciences, University of Liverpool, Liverpool, United Kingdom
4.Department of Oceanography, University of Hawai'i at Mānoa, Honolulu, HI, USA
5.School of Oceanography, University of Washington, Seattle, WA, USA
6.Columbia River Inter-Tribal Fish Commission, Portland, OR, USA
7.Centre for Ecology and Evolution in Microbial Model Systems, Linnaeus University, Kalmar, Sweden
8.Department of Oceanography, Dalhousie University, Halifax, Canada
9.Department of Mathematics and Statistics, Dalhousie University, Halifax, Canada
10.Daniel K. Inouye Center for Microbial Oceanography: Research and Education, University of Hawai'i at Mānoa, Honolulu, HI, USA
11.Ocean Sciences Department, Institute of Marine Sciences, University of California, Santa Cruz, Santa Cruz CA, USA

S1. Observations from SCOPE-Gradients Cruises

The three SCOPE-Gradients cruises (G1, G2, and G3) transited from Hawaii northward along 158^{o}W and returned along the same longitude (Fig. 1). G1 took place from 19 April to 4 May 2016 on the R/V Ka'imikai-O-Kanaloa, G2 from 25 May to 13 June 2017 on the R/V Marcus G. Langseth, and G3 from 9 to 30 April 2019 on the R/V Kilo Moana. G1 went to 38.7^{o}N, G2 to 42.3^{o}N, and G3 to 41.6^{o}N.

S1.1. Optical Instruments

Continuous underway flow-cytometer (SeaFlow) measurements were taken on all cruises, to estimate the biomass of small-size phytoplankton (nominally a diameter between 0.5 to 3 μm). Water from the ship's underway intake (5-7 m depth) is passed through a laser beam. Based on forward light scattering, as well as orange and red fluorescence, fluorescent phytoplankton cells are classified into four different populations: cyanobacteria *Prochlorococcus* and *Synechococcus*, the diazotroph *Crocosphaera*, and small eukaryotes (Fig. 2, Supplemental Fig. S2). Forward scattering signals are related to particle size through a Mie Theory model by assuming particle sphericity and specific indices of refraction of each population (Ribalet et al., 2019). For *Prochlorococcus*, the refractive index of 1.017 relative to the index of refraction of seawater for G1 and G2, and 1.032 during G3 were used in the Mie theory model as they resulted in the closest equivalent spherical diameter of 0.55 μm expected near station ALOHA (Casey et al., 2019). The refractive index of *Synechococcus* was assumed to the same as that for *Prochlorococcus*, while for *Crocosphaera* and small eukaryotes the refractive indices were kept at 1.054 for all cruises to provide conservative estimates of diameter for those populations, since little is known about how the bulk index of refraction of these populations vary in situ. Note however, that assuming a lower index of refraction for the eukaryote population would shift estimated diameters to larger sizes and thus increase the contribution of this population to the total biomass estimated by the instrument. Given the configurations chosen here, particles measured by the SeaFlow instrument were roughly constrained to the 0.5 - 3 μm size range. In this manuscript we refer to this 0.5-3 μm size range as "small" cells. Estimated SeaFlow cell diameters were converted to volume (V) assuming spherical particles and converted to carbon quotas (Q_c, units of fgC cell^{-1}) using the equation $Q_C = 0.261V^{0.860}$ (Ribalet et al., 2019). Cell counts and carbon quotas were used to calculate carbon biomass concentrations for each population.

Imaging FlowCytobot (IFCB; McLane Labs) was used to estimate the size and taxonomy of different phytoplankton during the G2 cruise. The IFCB uses flow cytometry together with video technology (Olson et al., 2003) to generate images of fluorescent and non-fluorescent cells from $\sim$ 3-100 μm in diameter. IFCB data were processed and annotated to the class level as in Juranek et al. (2020). Carbon concentrations for the particles in the IFCB size range were calculated following Menden-Deuer and Lessard (2000). We use these observations to determine total biomass of diatoms (Fig. 2f). We also use IFCB observations to determine the non-rare maximum sized phytoplankton at each latitude (Fig. 2a). Given that rare

larger cells are present, we determined the equivalent spherical diameter (ESD) at which 90% of the phytoplankton biomass is smaller sized. Varying this choice of percentage did not alter the pattern shown in Fig. 2a. The combination of the resolution of the IFCB, the photomultiplier settings, and weaker fluorescence signals of smaller cells can lead to decreased detection efficiency of particles near the low limit of the IFCB size range. Thus we used optically imaged estimates of biomass in different size classes from IFCB for cells over 5 μm, and SeaFlow biomass for smaller size classes. We note that there is potentially missing biomass between 3 and 5 μm not captured by either instrument (shown schematically in Supplemental Fig. S1).

Laser In Situ Scattering and Transmissometry sensor (LISST 100-X; Sequoia Scientific Inc.) was used for all three cruises to estimate particle size distributions across 32 logarithmically spaced bins centered between $\sim$ 1.25-100 μm using an inversion algorithm based on forward scattering measured at multiple angles. Raw scattering data provided by the LISST were converted to volume using the standard "spherical" kernel provided by the manufacturer (Sequoia Scientific) that is calculated using Mie theory as a composite of several indices of refraction, and is designed to produce accurate inversion results over a broad range of particle types (see White et al., 2015). Particle counts and carbon quotas were used to calculate bulk particulate organic carbon concentration (POC). Note that the LISST instrument does not differentiate between living and detrital particles, and neither between photosynthesizing and heterotrophic cells, and likely underestimates cells in the $<$ 1-3 μm range, as evidenced by the often observed non-linearity of the particle size distribution (White et al., 2015).

S1.2. Diazotroph gene counts

Discrete near-surface water samples were also collected for DNA sequence analysis during all three cruises. The small sublineage of the UCYN-A/haptophyte symbiosis (UCYN-A1) was quantified using quantitative PCR (qPCR) in G1 and G2 as described by Gradoville et al. (2020). For G3, sampling methodologies were the same as the previous two cruises, but UCYN-A1 was quantified using digital droplet PCR according to the methods of Gradoville et al. (2021). The qPCR and digital droplet PCR assays both used the UCYN-A1 primer/probe set described by Church et al. (2005).

S1.3. Determining the qualitative patterns of biogeography

To describe the biogeographical patterns of phytoplankton groups schematically as shown in Fig. 2g-l we employ the following procedure. Starting from the southernmost measurements and moving northward, we define the pattern as "uniform" if the subsequent poleward values deviated less than one standard deviation (of the full transect values). When deviations did exceed more than a standard deviation, we categorized these as an "increase" or "decrease", depending on the direction of the change. Additionally, if the variation was greater than 2 standard deviations we classified this as a "sharp" change. After each transition (increase or

decrease) we define a new baseline value. Subsequent polar increases/decreases were found relative to this new higher/lower biomass defined after the previous transition.

With these definitions we determine that *Prochlorococcus* had uniform distributions to the south in all three cruises (Fig. 2b,h). And in all three cruises there was a transition to no cells between 33^o and 36^oN, depending on the year, and in all cases these were "sharp". Before the transition to no cells, G1 and G2 had an initial increase from the southward uniform distribution. *Synechococcus* had low and uniform biomass in the southern part of the transect, increasing between 30^o and 34^oN and decreasing further again further north (Fig. 2c,j). The different cruises showed less consistency of what occurred at the northernmost part of the transects. In the south part of the transect, small eukaryotes biomass was uniform and of similar concentration as *Prochlorococcus* (Fig. 2d,j). Poleward (between about 36 to 38 ^{o}N) the biomass of this group increased significantly (and sharply in G2 and G3). After this initial large increase, the northernmost pattern was less consistent between cruises. The distribution of *nifH* gene-markers of UCYN-A1 was also relatively uniform to the south, and underwent a sharp decline between 28^o and 33^oN depending on the cruise (Fig. 2e,k). This pattern was also mirrored by the less abundant diazotroph, *Crocosphaera* (Gradoville et al., 2020, Supplemental Fig. S3). There are suggestions of isolated low abundances of *Crocosphaera* further north, as observed from cell counts, but also *nifH* genes (Gradoville et al., 2020). IFCB measurements, only available for G2, showed diatom distributions as low (uniformly) in the southern part of the transect, and increasing in the north (Fig. 2f). Previous cruises along similar transects also showed low diatom abundances in the subtropical portion, and significant abundances to the north (Bograd et al., 2004; Endo et al., 2018), and as such we feel the pattern is robust enough to show as in Figure 2l. The patterns of size classes are more difficult to determine given the complications of looking at biomass of photosynthesizing cells across a variety of instruments. However by eye, for SeaFlow and LISST on all three cruises, we see more larger biomass to the north of the transect (Supplemental Figs. S4) than the south. The combined used of SeaFlow and IFCB (Fig. 2a) for G2 shows this more clearly.

For the schematic depictions, we did not differentiate that the increases/decreases occurred at different latitudes between cruises, as these seasonal and interannual variability are not the focus of this study.

S2. Theoretical Framework

For clarity of explanation we have included the minimum number of plankton needed to describe the mechanisms effectively in Supplemental Tables S2 and S3 (symbols defined in Supplemental Table S1) and in schematic representations (e.g. Fig. 3). These theoretical frameworks can be expanded to systems of many plankton size classes or types.

S2.1. Detailed description of Mechanisms A-E

Mechanism A considers size-specific grazing and follows from previous studies (Armstrong, 1999; Ward et al., 2014; Dutkiewicz et al., 2020; Follows et al., 2018). Here we consider two size classes of phytoplankton P_j that compete for an inorganic resource (R_p, e.g. nitrate), and are each grazed by a different size class of zooplankton (Z_j). We assume here, and in other Mechanisms below, that the smallest phytoplankton, given its size has the highest nutrient affinity (Fiksen et al., 2013).In the absence of grazers the smaller phytoplankton (P_1), with this highest nutrient affinity, will draw down the resource (R_p, inorganic nutrient) to a level R^*_{p1} which is too low to support the less competitive larger phytoplankton. This is the case for very low resource supply rate, S_{Rp} (sector i, i.e. before the first dashed vertical line, in graph Fig. 3A). We now consider what happens as we move across a gradient of increasing nutrient supply (x-axis on plots in Fig. 3A). When resource supply rates are high enough to sustain sufficient P_1, a herbivorous zooplankton predator (Z_1) can also be supported. At this point, biomass concentration P_1 is capped and additional resources instead increase the zooplankton (Z_1) biomass (sector ii in Fig. 3A). However, at even higher resource supply, the steady state resource concentration R^*_{p1} (which is a function of zooplankton biomass, see Supplemental Table S3, Eq. SA1a) has increased enough to support the larger phytoplankton, P_2. This occurs when R^*_{p1} equals R^*_{p2} (Eqs. SA1a and SA1b, Insight SAI). At nutrient supply rates higher than this, the two sizes classes can co-exist (sector iii) , and with enough supply Z_2 can be supported and P_2 biomass is capped (sector iv). *Summary*: Size specific grazing allows an increase in the number of size classes that can co-exist along a transect of increasing resource supply rates, and sets a uniform distribution of each size class once it is under grazer control.

Mechanism B considers the impact of an additional trophic level, a carnivorous zooplankton (C_j) that grazers on the herbivorous zooplankton (Z_j). For low resource supply rates, the behavior follows as in Mechanism A, with zooplankton grazing maintaining phytoplankton biomass at a uniform concentration (Fig. 3B, sectors i and ii). But at a higher resource supply rate, Z_1 becomes high enough to support the next trophic level, the carnivore (see Supplemental Table S3, Insight SBI, sector iii in Fig. 3B). Above this resource supply rate, it is now the herbivorous zooplankton biomass that is maintained at uniform value. Without a strong grazer control, the phytoplankton biomass can now increase with higher resource supply rates. Here we show this mechanism for a single food chain, but similar explanation could be extended to a system with multiple size classes of food chains. We could also add additional trophic levels to this framework, with alternating patterns of uniform versus increasing phytoplankton biomass with increasing resource supply as each additional trophic level is added. This follows the odd-even food chain dynamics and trophic cascades previously discussed in ecosystem theory (Wollrab et al., 2012; Hairston et al., 1960; McCann and Yodzis, 1995). In fact, direct manipulation of upper trophic levels in lake systems has shown the surprisingly large impact on the base of the food web (Carpenter et al., 2001). *Summary*: When nutrient supply rates are high enough to support a third trophic level (carnivory), the release in grazing pressure allows phytoplankton biomass to increase.

Mechanism C considers the impact of a size class of phytoplankton sharing a grazer with a similar sized heterotrophic bacteria (H_j) that consumes organic matter (R_h) and remineralizes that matter back to inorganic nutrients. We considered a similar framework in Follett et al. (2022), though here we explicitly include in addition a heterotrophic bacteria (H_0) that is smaller than the smallest phytoplankton, as well as its grazer (Z_0). Phytoplankton consume the inorganic nutrient (R_p) and produce the organic resource (R_h) that fuels the heterotrophic bacteria. As total plankton biomass increases along a gradient of inorganic resource supply rate the supply of the organic resource also increases. At lower rates there is only enough organic matter to support the smallest bacteria (H_0, assumed to have highest organic resource affinity; sector $i-iv$ in Fig. 3C), but in a similar mechanism as described in Mechanism A (there for phytoplankton), with higher organic resource supply rates the larger bacteria (H_1) can be supported (sectors v and vi). But the theory suggests that it is the combined biomass of P_1 and H_1 that is set at a uniform concentration (Supplemental Table S3, Eq SC3). Thus, as biomass of H_1 increases with higher supply rates of inorganic and organic resources P_1 biomass must decrease (sector v). When resource supply rates are even higher P_1 biomass eventually reaches zero (sector vi). This mechanism of shared predation is also known as "apparent competition" as studied in terrestrial and tidal systems (Holt, 1977; Holt and Bonsall, 2017). *Summary*: Shared predation with a similar sized heterotrophic bacterium can lead to the decline and eventual collapse of a phytoplankton size class with increasing supply of inorganic (and hence organic) resource.

Mechanism D considers a marine food web (as opposed to the food chains explored in the previous Mechanisms), where multiple zooplankton can graze on a single phytoplankton size class. We call this "cross-size class grazing", and introduce the symbol ϕ which describes the degree of palatability (preferred prey $\phi = 1$, less preferred prey has $\phi < 1$). Though Z_1 preferentially grazes on P_1, we now allow Z_1 to also graze on P_2, though with lower preference (denoted by ϕ <1, Supplemental Table S3). Similarly, the larger zooplankton Z_2 preferentially grazes on the larger phytoplankton P_2, but it also grazes on P_1 with lower preference. At low resource supply rates only P_1 and Z_1 are supported and the patterns follow those of Mechanism A (Fig. 3D, sectors i and ii). However, once the supply rate supports P_2, P_1 decreases (sector iii): Shared grazing by the single zooplankton leads to a cap in the combined biomass of the two phytoplankton. Once there is enough resource supply for Z_2 to be supported (sector iv), then P_1 and P_2 can coexist if certain constraints are met relative to their respective grazers' grazing rates and the value of ϕ (Supplemental Table S3, Insight DI). High ϕ and large differences between the two grazing rates will lead to exclusion of the phytoplankton with the grazer with higher maximum grazing rate (Supplemental Fig. S6). If they do coexist, P_1 and P_2 have uniform concentrations across higher resource supply rates, but at lower concentration than if there were no cross-grazing (Supplemental Table S3, Eqs SD2 and SD3 relative to Eqs SA2 and SA3). The relative abundance of P_1 to P_2 is set by which grazer has the higher grazing rate (Insight SDII). For instance, if Z_1 grazing rate is higher than Z_2, then P_1 will have lower concentration than P_2 and vice versa. *Summary*: Shared predation though cross-size class grazing alters the relative abundance of different size classes, and can lead to the exclusion of one size class.

Mechanism E considers impact of different limiting inorganic resources (R_{pi}) where the i could denote nitrate, phosphate, or iron. In these equations two phytoplankton (that could be of similar size or not) are limited by different nutrients X and Y. P_1 is assumed as the faster grower and limited by resource X, though also requires Y, and the slower grower is only limited by resource Y. Υ_{ij} (j=1,2) is the stoichmetric requirements for each plankton for resource i relative to a common currency (e.g. carbon), and here P_j has units of this common currency. This mechanism has been explored previously (Follows et al., 2018; Dutkiewicz et al., 2020; Ward et al., 2013; Dutkiewicz et al., 2014) for the ability of slower growing nitrogen fixers (P_2) to co-exist with faster growing non-diazotrophs (P_1), where X is DIN, and Y could be iron or phosphate. In this case we assume diazotrophs fix all required nitrogen. This mechanism has also been explored (Dutkiewicz et al., 2020) for slower growing non-diatoms (P_2) to co-exist with faster growing diatoms (P_1) when the latter are limited by silicic acid (resource X in this case).

S2.2. Strength and Limitation of Theoretical Frameworks

The mechanisms described above are general, but the mathematical predictions have been made by assuming a steady state. We know that the real ocean is a dynamic environment, but steady state solutions can provide insightful predictions across much of the ocean (Dutkiewicz et al., 2009) while being straightforward to interpret. Steady state approximations appear to be useful to explain systems in lower latitudes (equatorward of about 40^o), higher latitude summers (Dutkiewicz et al., 2009), and potentially for annual average patterns (Ward et al., 2014). Simple predictions can also be made for some non-steady state conditions like the spring bloom (Dutkiewicz et al., 2009, 2020). Those calculations suggest a successional pattern. The fastest grower will dominate until its grazer catches up with sufficient biomass, or it runs out of key resources. The next fastest growing phytoplankton or one with different nutrient requirements can then grow in and co-exist (see e.g. appendix of Dutkiewicz et al., 2020). Thus, we anticipate that our steady state explanations are broadly applicable to much of the SCOPE-Gradient transects, whose furthest poleward extent was 40^oN. Starting at the very northern edge of the transects, time-dependent theory accounting for seasonal bloom dynamics would be required.

S3. Numerical Model

S3.1. Model Description

We use the Darwin ecosystem model configured to include the cycling of carbon, nitrogen, phosphorus, silica, iron and oxygen through inorganic, dissolved and particular detrital pools and 50 plankton types (Fig. 4). There are 24 autotroph types, 7 mixotroph types, 16 zooplankton, and 3 types of heterotrophic bacteria. The model is trait-based in that it defines

the plankton types in terms of traits: size, trophic strategy, nutrient requirements, rather than attempting to model specific species. The phytoplankton span across 15 size classes ranging from 0.6 mm to 104 μm equivalent spherical diameter (ESD). The phytoplankton are additionally split into functional groups including diatoms, other nano phytoplankton (based on coccolithophores), prokaryotes, pico-eukaryotes ($<2\mu$m), diazotrophs, and mixotrophic dinoflagellates. Though the model is trait-based, the smallest phytoplankton (with ESD of 0.6 μm) can be thought of as an analog of *Prochlorococcus*, and the second smallest (ESD 0.9μm) as an analog of *Synechococcus*, given that these species are unique to these size classes. Phytoplankton growth parameters are allometrically defined, with functional group specifics (Dutkiewicz et al., 2020). Growth rates are unimodal with size (i.e. highest for small nanophytoplankton) as suggested by laboratory observations (see e.g. Marañón et al., 2013; Dutkiewicz et al., 2020). Growth rates are also a function of multiple potential limiting nutrients (dissolved inorganic nitrogen, phosphate, iron, and silicic acid), spectral light, photoacclimation, and temperature. The zooplankton range from 4.5 to 1600 μm and graze on plankton (either phyto, mixo or heterotrophic) 5 to 15 times smaller than themselves, but, preferentially, 10 times smaller (Hansen et al., 1994; Fenchel, 1987; Kiørboe, 2019). We use a Holling II (Holling, 1965) saturation grazing function. (Note that this is different to the linear, Holling I, parameterization in the theoretical frameworks, Supplemental Table S2. In the theoretical framework, the linear parameterization was used such that the equations could be solved analytically and more easily understood.) The three heterotrophic bacteria, range from smaller than to the same size as the two smallest phytoplankton. This complex ecosystem, along with inorganic, dissolved, and particulate material, is advected and mixed within a three-dimensional global ocean model (MITgcm, Marshall et al., 1997) constrained to be consistent with altimetric and hydrographic observations (Wunsch and Heimbach, 2007). The horizontal resolution of the model is 1^o, and ranges in the vertical from 10 m at the surface to 500 m at its deepest. The model is run for 10 years, a stable repeating ecosystem spatial and temporal pattern develops within 3 years, and we show results from the final year. This model setup was previously used in Follett et al. (2022), and the large-scale global distribution and seasonality of bulk ecosystem properties such as Chl *a*, as well as distributions of size classes and functional groups, are plausible in comparison with satellite and in situ observations (see supplement of Follett et al., 2022).

S3.2. Calculation Nutrient Fluxes

Nutrient supply rates (Fig. 1f, Supplemental Fig. S10) were calculated as all sources and sinks of the nutrients into the top 50 m of the water column at each location. These included advection both laterally and vertically, mixing, remineralization of organic matter, and in the case of iron, aeolian sources.

S3.3. Sensitivity experiments:

EXP-A: single generalist grazer. This experiment was designed to explore Mechanism A and how size-dependent grazing allows for multiple size classes to co-exist. In EXP-A, instead of a range of size classes of zooplankton (as in EXP-0), we have a single zooplankton type that grazes indiscriminately on all size classes of plankton. We also remove the capability of mixotrophy to ensure no size-specific grazing pressure. A similar experiment was done in Dutkiewicz et al. (2020), and as in that experiment the number of size classes that co-exist drops dramatically (Fig. 5b, right panel), suggesting that this mechanism is important in maintaining size diversity. However, the number of size classes does not reduce to just the smallest, indicating that other mechanisms can also maintain some level of size diversity. Different limiting nutrients (Mechanism E) allows for co-existence of diazotrophs (which are all larger than 2 μm ESD, see Fig. 4) with the smaller phytoplankton in the southern part of the Transition (see EXP-Ea below), and pico-eukaryotes and diatoms co-exist in the northern part of the region. Seasonality in the northern portion of the region breaks the steady-state assumption of the theory and allows for the fastest growing type (a diatom) to dominate during the spring bloom (see discussions in Dutkiewicz et al., 2020; Follows et al., 2018). Pico-eukaryotes (whose maximum growth rate is faster than the pico-cyanobacteria, i.e. *Prochlorococcus* and *Synechococcus*) can exist in the north when silica becomes limiting and the south when the grazing pressure is too high to maintain the slower growing pico-cyanobacteria. The exact patterns are set by the maximum grazing rate chosen for the single grazer. This experiment suggests that though size-specific grazing is a crucial component of size class co-existence, other mechanisms can also play important roles.

EXP-B: no third trophic level. This experiment was designed to explore whether carnivory allows for increases in biomass as observed for some phytoplankton types across the transect (e.g. pico-eukaryotes, Fig. 2d). In EXP-B we do not allow zooplankton to graze on other zooplankton (e.g. removing all the curved arrows in Fig. 4). In this experiment modelled pico-eukaryote biomass is almost uniform across the entire region without carnivory (Fig. 5c), in sharp contrast to the default experiment with carnivory (EXP-0). The patterns of all the pico-cyanobacteria are also more uniform in this experiment. These results suggest that small carnivores (technically omnivores in the model, as they also graze on phytoplankton) play a large role in the increases of these small phytoplankton observed in the northern part of the Transition Zone. However, diazotroph patterns do not change much between experiments (since their pattern is set by differing limiting nutrients, Mechanism E). Diatom patterns also remain largely unaffected as their pattern is set by silicic acid availability (see later experiments), and by strong seasonality in the northern portion of this region.

EXP-C: no explicit bacteria. This experiment was designed to show that shared grazing with a similar sized heterotrophic bacterium could lead to the collapse of *Prochlorococcus* (Mechanism C), and similar results have previously been shown in Follett et al. (2022). In EXP-C, bacteria are not modelled explicitly, but rather remineralization is treated as a rate dependent process. In this experiment, without sharing a grazer with bacteria, *Prochlorococcus* exists across the entire domain (Fig. 5d). In regions where *Prochloroccocus*

had no biomass in the default experiment (EXP0), *Synechococcus* and pico-eukaryote biomass decreased in response (Fig. 5b, Supplemental Fig. S8d). But also noticeable is that in the far north *Synechococcus* biomass increases significantly in EXP-C too, suggesting that shared grazing with the largest heterotrophic bacteria also limits the *Synechococcus* domain.

EXP-D: cross-size class grazing. In the default experiment, grazers preferentially ($\phi = 1$) grazed on prey 10 times smaller than themselves, but also grazed on one size class smaller and larger with preference of $\phi = 0.3$. We consider the impact of increasing the cross-size grazing, $\phi = 0.6$, in EXP-D1 and removing any cross-size grazing ($\phi = 0$) in EXP-D2 (Fig. 5e and Supplemental Figs. S7, S8, S9). *Synechococcus* biomass decreased with the higher cross-grazing (EXP-D1) and more in line with observations. *Prochlorococcus* and pico-eukaryotes biomass increase (Supplemental Fig. S8). The localization of peaks in biomass in some size classes, along with complete removal of other size classes, has been noted in previous modelling studies (Banas, 2011; Moscoso et al., 2022). In those studies, this "quantization" in the size spectrum was linked to the size selectivity of the predation. Here, we believe that the relatively low biomass of *Synechococcus* in the observations could be an example of this quantization. Further work is needed to determine the best parametrization of this cross-size grazing for future versions of our model to better capture *Synechococcus*-analogs. It is also notable that the latitude of the *Prochlorococcus* biomass decline is altered in these experiments (horizontal dashed lines in Supplemental Fig. S7). These experiments suggest that the exact location of the decline in *Prochlorococcus* is additionally impacted by cross-grazing with other size classes of phytoplankton (Mechanism D).

EXP-Ea: altered iron supply. Diazotrophs in the default simulation are found where there is excess supply of iron (and phosphate) relative to non-diazotroph needs (see Supplemental Fig. S10e,f). We conduct two experiments (EXP-Ea1 and EXP-Ea2) where we halve or double the amount of iron dust that reaches the ocean respectively (Fig. 5f, Supplemental Figs. S8, S11). This effectively alters the ratio of supply rates of Fe to N ($S_{Fe} : S_N$) and we see (as in past studies, e.g. Dutkiewicz et al., 2014, 2012) that this dramatically changes the biogeography of diazotrophs (Fig. 5f). In the case of reduced iron dust (EXP-Ea1), there are fewer regions where the ratio of supplies is larger than the non-diazotroph requirements for these two resources, and hence the region where diazotrophy occurs is decreased. In particular, the lack of diazotrophy in the southern portion of the region in EXP-Ea1 is at odds with the observations (Fig. 2e). This suggests that the shift from excess iron supply in the southern part of the transect to limited availability of iron relative to DIN in the northern part (Mechanism E) could be responsible for the sharp decrease observed in G1, G2, and G3 (Fig. 2e). There are also fewer size classes in the southern portion of the region in this experiment (right most panel in Fig. 5f) suggesting the importance of multiple limiting nutrients in maintaining size diversity. When we double the iron supply (EXP-Ea2), the diazotroph distribution expands, but diazotroph biomass decreases in some regions where phosphate becomes limiting (Supplemental Fig. S11c, see also Ward et al., 2013; Dutkiewicz et al., 2014). Note that reduced iron input (EXP-Ea1) decreases diatom biomass in the equatorial Pacific which allows more silicic acid to reach the southern portion of our region, leading to increased diatoms there (Supplemental Fig. S11); opposite results occur in EXP-Ea2.

EXP-Eb: altered silica requirements for diatoms. Though EXP-Ea already shows the importance of silicic acid supply for setting diatom distribution, we additionally consider two experiments where we alter the stoichiometric demands for silica relative to nitrogen (γ_{SiN}) for diatoms (EXP-Eb1, halved and EXP-Eb2, doubled). Lower γ_{SiN} (EXP-Eb1) leads to more diatoms (Fig. 5g, Supplemental Figs. S8g and S12). With less utilization of silicic acid in the north, more of this nutrient is transported southward across the region and there is a subsequent extension of the diatom's spatial distribution. Opposite patterns are seen in EXP-Eb2. These experiments (and EXP-Ea) suggest that supply of silicic acid is the main controlling mechanism for diatom distributions.

References

Armstrong, R.A., 1999. Stable model structures for representing biogeochemical diversity and size spectra in plankton communities. Journal of Plankton Research 21 (3), 445–464. doi: 10.1093/plankt/21.3.445

Banas, N.S., 2011. Adding complex trophic interactions to a size-spectral plankton model: emergent diversity patterns and limits on predictability. Ecological Modelling 222 (15), 2663–2675.

Bograd, S.J., Foley, D.G., Schwing, F.B., Wilson, C., Laurs, R.M., Polovina, J.J., Howell, E.A. and Brainard, R.E., 2004. On the seasonal and interannual migrations of the transition zone chlorophyll front. Geophysical Research Letters 31 (17). doi: 10.1029/2004GL020637

Carpenter, S.R. and others, 2001. Trophic cascades, nutrients, and lake Pproductivity: Whole-lake experiments. Ecological Monographs 71. doi: doi:10.2307/2657215

Casey, J.R., Björkman, K.M., Ferrón, S. and Karl, D.M., 2019. Size dependence of metabolism within marine picoplankton populations. Limnology and Oceanography 64, 1819–1827. doi: 10.1002/lno.11153

Church, M., Jenkins, B., Karl, D. and Zehr, J., 2005. Vertical distributions of nitrogen-fixing phylotypes at Stn ALOHA in the oligotrophic North Pacific Ocean. Aquatic Microbial Ecology 38, 3–14.

Dutkiewicz, S., Cermeño, P., Jahn, O., Follows, M.J., Hickman, A.A., Taniguchi, D.A.A. and Ward, B.A., 2020. Dimensions of marine phytoplankton diversity. Biogeosciences 17 (3), 609–634. doi: 10.5194/bg-17-609-2020

Dutkiewicz, S., Follows, M.J. and Bragg, J.G., 2009. Modeling the coupling of ocean ecology and biogeochemistry. Global Biogeochemical Cycles 23 (4), GB4011. doi: 10.1029/2008GB003405

Dutkiewicz, S., Ward, B.A., Monteiro, F. and Follows, M.J., 2012. Interconnection of nitrogen fixers and iron in the Pacific Ocean: Theory and numerical simulations. Global Biogeochemical Cycles 26 (1), GB1012. doi: 10.1029/2011GB004039

Dutkiewicz, S., Ward, B.A., Scott, J.R. and Follows, M.J., 2014. Understanding predicted shifts in diazotroph biogeography using resource competition theory. Biogeosciences 11 (19), 5445–5461. doi: 10.5194/bg-11-5445-2014

Endo, H., Ogata, H. and Suzuki, K., 2018. Contrasting biogeography and diversity patterns between diatoms and haptophytes in the central Pacific Ocean. Science Reports 8, 10916. doi: doi:10.1038/s41598-018-29039-9

Fenchel, T., 1987. Ecology - potentials and limitations. Excellence in Ecology: Book 1. Ecological Institute, D-1224 Oldendorf/Luhe, Fedral Republic of Germany.

Fiksen, Ø., Follows, M. and Aksnes, D.L., 2013. Trait-based models of nutrient uptake in microbes extend the Michaelis-Menten framework. Limnology Oceanography 58, 193–202. doi: doi:10.4319/lo.2013.58.1.0193

Follett, C.L., Dutkiewicz, S., Forget, G., Cael, B.B. and Follows, M.J., 2021. Moving ecological and biogeochemical transitions across the North Pacific. Limnology and Oceanography 66, lno.11763. doi: 10.1002/lno.11763

Follett, C.L., Dutkiewicz, S., Ribalet, F., Zakem, E., Caron, D., Armbrust, E.V. and Follows, M.J., 2022. Trophic interactions with heterotrophic bacteria limit the range of *Prochlorococcus*. Proceedings of the National Academy of Sciences of the United States of America 119 (2), e2110993118. doi: 10.1073/pnas.2110993118

Follows, M.J., Dutkiewicz, S., Ward, B. and Follett, C., 2018. Theoretical interpretations of subtropical plankton biogeography. In: Gasol, J. and Kirchman, D. (Eds.), Microbial Ecology of the Oceans, 3rd Edition. John Wiley & Sons, Ltd, Hoboken, NJ, p. 467.

Gradoville, M.R., Cabello, A.M., Wilson, S.T., Turk-Kubo, K.A., Karl, D.M. and Zehr, J.P., 2021. Light and depth dependency of nitrogen fixation by the non-photosynthetic, symbiotic cyanobacterium UCYN-A. Environmental Microbiology 23 (8), 4518–4531. doi: doi:10.1111/1462-2920.15645

Gradoville, M.R. and others, 2020. Latitudinal constraints on the abundance and activity of the cyanobacterium UCYN-A and other marine diazotrophs in the North Pacific. Limnology and Oceanography 65 (8), 1858–1875. doi: 10.1002/lno.1143

Hairston, N.G., Smith, F.E. and Slobodkin, L.B., 1960. Community structure, population control, and competition. The American Naturalist 94 (879), 421–425. doi: 10.1086/282146

Hansen, B., Bjornsen, P.K. and Hansen, P.J., 1994. The size ratio between planktonic predators and their prey. Limnology and Oceanography 39 (2), 395–403. doi: doi:10.4319/lo.1994.39.2.0395

Holling, C.S., 1965. The Functional Response of Predators to Prey Density and its Role in Mimicry and Population Regulation. Memoirs of the Entomological Society of Canada 97 (S45), 5–60. doi: 10.4039/entm9745fv

Holt, R.D., 1977. Predation, Apparent Competition, and the Structure of Prey Communities. Theoretical Population Biology 12, 197–229.

Holt, R.D. and Bonsall, M.B., 2017. Apparent Competition. Annual Review of Ecology, Evolution, and Systematics 48, 447–471. doi: 10.1146/annurev-ecolsys-110316-022628

Juranek, L.W. and others, 2020. The importance of the phytoplankton "middle class" to ocean net community production. Global Biogeochemical Cycles 34 (12), e2020GB006702. doi: 10.1029/2020GB006702

Kiørboe, T., 2019. A Mechanistic Approach to Plankton Ecology. Princeton University Press. doi: 10.1515/9780691190310

Marañón, E., Cermeño, P., López-Sandoval, D.C., Rodríguez-Ramos, T., Sobrino, C., Huete-Ortega, M., Blanco, J.M. and Rodríguez, J., 2013. Unimodal size scaling of phytoplankton growth and the size dependence of nutrient uptake and use. Ecology Letters 16 (3), 371–379. doi: 10.1111/ele.12052

Marshall, J., Adcroft, A., Hill, C., Perelman, L. and Heisey, C., 1997. A finite-volume, incompressible navier stokes model for, studies of the ocean on parallel computers. Journal of Geophysical Research C: Oceans 102 (C3), 5753–5766. doi: 10.1029/96JC02775

McCann, K. and Yodzis, P., 1995. Biological conditions for chaos in a three-species food chain. Ecology 75, 561–564.

Menden-Deuer, S. and Lessard, E.J., 2000. Carbon to volume relationships for dinoflagellates, diatoms, and other protist plankton. Limnology and Oceanography 45 (3), 569–579. doi: doi:10.4319/lo.2000.45.3.0569

Moscoso, J.E., Bianchi, D. and Stewart, A.L., 2022. Controls and characteristics of biomass quantization in size-structured planktonic ecosystem models. Ecological Modelling 468, 109907. doi: doi:10.1016/j.ecolmodel.2022.109907

Olson, R.J., Shalapyonok, A. and Sosik, H.M., 2003. An automated submersible flow cytometer for analyzing pico-and nano-phytoplankton: FlowCytobot. Deep-Sea Research Part I: Oceanographic Research Papers 50, 301–315. doi: doi:10.1016/S0967-0637(03)00003-7

Ribalet, F., Berthiaume, C., Hynes, A. and et al., 2019. SeaFlow data v1, high-resolution abundance, size and biomass of small phytoplankton in the North Pacific. Scientific Data 6, 277. doi: doi:10.1038/s41597-019-0292-2

Ward, B.A., Dutkiewicz, S. and Follows, M.J., 2014. Modelling spatial and temporal patterns in size-structured marine plankton communities: Top-down and bottom-up controls. Journal of Plankton Research 36 (1), 31–47. doi: doi:10.1093/plankt/fbt097

Ward, B.A., Dutkiewicz, S., Moore, C.M. and Follows, M.J., 2013. Iron, phosphorus, and nitrogen supply ratios define the biogeography of nitrogen fixation. Limnology and Oceanography 58 (6), 2059–2075. doi: doi:10.4319/lo.2013.58.6.2059

White, A., Whitmire, A., Barone, B., Letelier, R., Karl, D. and Church, M., 2015. Phenology of particle size distributions in the North Pacific gyre. Journal of Geophysical Research-Oceans 120, 7381–7399. doi: doi: 10.1002/2015JC010897

Wollrab, S., Diehl, S. and Roos, A.M.D., 2012. Simple rules describe bottom-up and top-down control in food webs with alternative energy pathways. Ecology Letters 15, 935–946.

Wunsch, C. and Heimbach, P., 2007. Practical global oceanic state estimation. Physica D: Nonlinear Phenomena 230 (1-2), 197–208. doi: 10.1016/j.physd.2006.09.040

symbol	definition	units
R_p	inorganic resource concentration	mmol m^{-3}
R_h	organic resource concentration	mmol m^{-3}
P_j	biomass of j-th phytoplankton type	mmol m^{-3}
Z_j	biomass of j-th zooplankton type	mmol m^{-3}
C_j	biomass of j-th carnivore type	mmol m^{-3}
H_j	biomass of j-th heterotrophic bacteria type	mmol m^{-3}
S_{R_p}	rate of supply of inorganic resource, R_p	mmol m^{-3} s^{-1}
S_{R_h}	rate of supply of organic resource, R_h	mmol m^{-3} s^{-1}
$\mu_{pj} = \frac{\mu_{pj}^{max} R_p}{R_p + \kappa_{pj}}$	growth rate of j-th phytoplankton type	s^{-1}
μ_{pj}^{max}	maximum growth rate of j-th phytoplankton	s^{-1}
κ_{pj}	half saturation constant for inorganic resource	mmol m^{-3}
g_{zj}	per biomass grazing rate for j-th zooplankton	m^3 $mmol^{-1}$ s^{-1}
g_{ci}	per biomass grazing rate for j-th carnivore	m^3 $mmol^{-1}$ s^{-1}
γ	grazing efficiency	unitless
m_p	linear loss rate for phytoplankton	s^{-1}
m_z	linear loss rate for zooplankton	s^{-1}
m_c	linear loss rate for carnivore	s^{-1}
m_h	linear loss rate for heterotrophic bacteria	s^{-1}
$\mu_{hj} = \frac{\mu_{hj}^{max} R_h}{R_h + \kappa_{hj}}$	rate bacteria consumes organic matter	s^{-1}
μ_{hj}^{max}	maximum consumption rate of j-th bacteria	s^{-1}
κ_{hj}	half saturation constant for organic resource	mmol m^{-3}
δ	yield from bacterial consumption	unitless
ϕ	palatability of j-th phytoplankton by non-j-th zooplankton	unitless
$S_{R_p i}$	rate of supply of i-th inorganic resource, R_{pi}	mmol m^{-3} s^{-1}
Υ_{XYj}	stoichiometric ratio requirements for phytoplankton j for element X and Y	mmol X (mmol Y)$^{-1}$
$\mu_{pij} = \frac{\mu_{pj}^{max} R_i}{R_i + \kappa_{ij}}$	growth rate of j-th phytoplankton type when limited by resource i	s^{-1}

Supplemental Table S1: Symbols used in Theoretical Frameworks, equations in Supplemental Table S2, steady state results in Supplemental Table S3, also see Figure 3.

Mechanism A		Size-specific grazing (Armstrong, 1999; Ward et al., 2014; Dutkiewicz et al., 2020; Follows et al., 2018)
$\frac{dR_p}{dt}$	=	$-\mu_{p1}P_1 - \mu_{p2}P_2 + S_{R_p}$
$\frac{dP_1}{dt}$	=	$+\mu_{p1}P_1 - g_{z1}P_1Z_1 - m_pP_1$
$\frac{dP_2}{dt}$	=	$+\mu_{p2}P_2 - g_{z2}P_2Z_2 - m_pP_2$
$\frac{dZ_1}{dt}$	=	$+\gamma g_{z1}P_1Z_1 - m_zZ_1$
$\frac{dZ_2}{dt}$	=	$+\gamma g_{z2}P_2Z_2 - m_zZ_2$
Mechanism B		Third trophic level
$\frac{dR_p}{dt}$	=	$-\sum \mu_{p1}P_1 + S_{R_p}$
$\frac{dP_1}{dt}$	=	$+\mu_{p1}P_1 - g_{z1}P_1Z_1 - m_pP_1$
$\frac{dZ_1}{dt}$	=	$+\gamma g_{z1}P_1jZ_1 - g_{c1}C_1 - m_zZ_1$
$\frac{dC_1}{dt}$	=	$+\gamma g_{c1}Z_1C_1 - m_zC_1$
Mechanism C		Shared grazing with bacteria (Follett et al., 2022)
$\frac{dR_p}{dt}$	=	$-\mu_{p1}P_1 - \mu_{p2}P_2 + S_{R_p}$
$\frac{dP_1}{dt}$	=	$+\mu_{p1}P_1 - g_{z1}P_1Z_1 - m_pP_1$
$\frac{dP_2}{dt}$	=	$+\mu_{p2}P_2 - g_{z2}P_2Z_2 - m_pP_2$
$\frac{dH_0}{dt}$	=	$+\mu_{h0}H_0 - g_{z0}H_0Z_0 - m_hH_0$
$\frac{dH_1}{dt}$	=	$+\mu_{h1}H_1 - g_{z1}H_1Z_1 - m_hH_1$
$\frac{dZ_0}{dt}$	=	$+\gamma g_{z0}H_0Z_0 - m_zZ_0$
$\frac{dZ_1}{dt}$	=	$+\gamma g_{z1}(P_1 + H_1)Z_1 - m_zZ_1$
$\frac{dZ_2}{dt}$	=	$+\gamma g_{z2}P_2Z_2 - m_zZ_2$
$\frac{dR_h}{dt}$	=	$-\delta\mu_{h0}H_0 - \delta\mu_{h1}H_1 + S_{R_h}$
Mechanism D		Shared grazing with other size classes
$fracdR_pdt$	=	$-\mu_{p1}P_1 - \mu_{p2}P_2 + S_{R_p}$
$\frac{dP_1}{dt}$	=	$+\mu_{p1}P_1 - g_{z1}P_1Z_1 - \phi g_{z2}P_1Z_2 - m_pP_1$
$\frac{dP_2}{dt}$	=	$+\mu_{p2}P_2 - \phi g_{z1}P_2Z_1 - g_{z2}P_2Z_2 - m_pP_2$
$\frac{dZ_1}{dt}$	=	$+\gamma g_{z1}(P_1Z_1 + \phi P_2Z_1) - m_zZ_1$
$\frac{dZ_2}{dt}$	=	$+\gamma g_{z2}(\phi P_1Z_2 + P_2Z_2) - m_zZ_2$
Mechanism E		Different limiting resource (Follows et al., 2018; Dutkiewicz et al., 2020; Ward et al., 2013; Dutkiewicz et al., 2014)
$\frac{dR_X}{dt}$	=	$-\mu_{p1_X}\Upsilon_{X1}P_1 + S_{R_X}$
$\frac{dR_Y}{dt}$	=	$-\mu_{p1_X}\Upsilon_{Y1}P_1 - \mu_{p2_Y}\Upsilon_{Y2}P_2 + S_{R_Y}$
$\frac{dP_1}{dt}$	=	$+\mu_{p1_X}P_1 - m_pP_1$
$\frac{dP_2}{dt}$	=	$+\mu_{p2_Y}P_2 - m_pP_2$

Supplemental Table S2: Differential equations for the theoretical frameworks listed Mechanism A through E. Cartoon of each framework are shown in shaded portions of Figure 3. Symbols are given in Supplemental Table S1 and the steady-state solutions in Supplemental Table S3.

Mechanism A		Size-specific grazing (Armstrong, 1999; Ward et al., 2014; Dutkiewicz et al., 2020; Follows et al., 2018)	**Eq**
R^*_{p1}	=	$\frac{\kappa_1(m_p+g_{z1}Z^*_1)}{\mu^{max}_{p1}-(m_p+g_{z1}Z^*_1)}$; R^*_{p2} = $\frac{\kappa_2(m_p+g_{z2}Z^*_2)}{\mu^{max}_{p2}-(m_p+g_{z2}Z^*_2)}$	SA1a,b
P^*_1	=	$\frac{m_z}{\gamma g_{z1}}$	SA2
P^*_2	=	$\frac{m_z}{\gamma g_{z2}}$	SA3
$Z^*_1 + Z^*_2$	=	$\frac{\gamma}{m_z}S^*_{R_p} - m_p(\frac{1}{g_{z1}} + \frac{1}{g_{z2}})$	SA4
Insight SAI:		P_1 and P_2 co-exist if $S^*_{R_P} > \frac{m_z}{\gamma g_{z1}}\frac{\mu^{max}_{p1}m_pk_2}{\mu^{max}_{p2}+m_p(k_2-k_1)}$	
Insight SAII:		P_j uniform concentration with increasing S_{R_p} once Z_j exists	
Mechanism B		Third trophic level	
R^*_{p1}	=	$\frac{\kappa_1(m_p+\frac{g_{z1}m_c}{\gamma g_{c1}})}{\mu^{max}_{p1}-(m_p+\frac{g_{z1}m_c}{\gamma g_{c1}})}$	SB1
P^*_1	=	$\frac{m_z}{\gamma g_{z1}} + C^*_1$	SB2
Z^*_1	=	$\frac{m_c}{\gamma g_{c1}}$	SB3
C^*_1	=	$\frac{\gamma^2 g_{c1}}{m_c g_{z1}+m_p\gamma^2 g_{c1}}(S^*_{R_p} - \frac{m_z}{\gamma}(\frac{m_c}{\gamma g_{c1}} + \frac{m_p}{g_{z1}}))$	SB4
Insight SBI:		C_1 exists if $S_{R_p} > \frac{m_z}{\gamma}(\frac{m_c}{\gamma g_{c1}} + \frac{m_p}{g_{z1}}))$	
Insight SBII:		P_1 increases with increasing S_{R_p} once C_1 exists	
Mechanism C		Shared grazing with bacteria (Follett et al., 2022)	
R^*_{p1}	=	$\frac{\kappa_{p1}(m_p+g_{z1}Z^*_1)}{\mu^{max}_{p1}-(m_p+g_{z1}Z^*_1)}$; R^*_{p2} = $\frac{\kappa_2(m_p+g_{z2}Z^*_2)}{\mu^{max}_{p2}-(m_p+g_{z2}Z^*_2)}$	SC1a,b
H^*_0	=	$\frac{m_z}{\gamma g_{z0}}$	SC2
$P^*_1 + H^*_1$	=	$\frac{m_z}{\gamma g_{z1}}$	SC3
P^*_2	=	$\frac{m_z}{\gamma g_{z2}}$	SC4
$Z^*_0 + Z^*_1 + Z^*_2$	=	$\frac{\gamma}{m_z}(S^*_{R_p} + \frac{S^*_{R_h}}{\delta}) - m_p(\frac{1}{g_{z0}} + \frac{1}{g_{z1}} + \frac{1}{g_{z2}})$	SC5
R^*_{h0}	=	$\frac{\kappa_{h0}(m_h+g_{z0}Z^*_0)}{\mu^{max}_{h0}-(m_h+g_{z0}Z^*_0)}$; R^*_{h1} = $\frac{\kappa_{h1}(m_h+g_{z1}Z^*_1)}{\mu^{max}_{h1}-(m_h+g_{z1}Z^*_1)}$	SC6a,b
Insight SCI:		$P_1 = 0$ once S_{R_p} sufficient for H_1 to reach biomass of $\frac{m_z}{\gamma g_{z1}}$	
Mechanism D		Shared grazing with other size classes	
R^*_{p1}	=	$\frac{\kappa_{p1}(m_p+g_{z1}Z^*_1+\phi g_{z2}Z^*_2)}{\mu^{max}_{p1}-(m_p+Z^*_1+\phi g_{z2}Z^*_2)}$; R^*_{p2} = $\frac{\kappa_{p2}(m_p+\phi g_{z1}Z^*_1+g_{z2}Z^*_2)}{\mu^{max}_{p2}-(m_p+\phi g_{z1}Z^*_1+g_{z2}Z^*_2)}$	SD1a,b
P^*_1	=	$\frac{1}{1-\phi^2}\frac{m_z}{\gamma}(\frac{1}{g_{z1}} - \frac{\phi}{g_{z2}})$	SD2
P^*_2	=	$\frac{1}{1-\phi^2}\frac{m_z}{\gamma}(\frac{1}{g_{z2}} - \frac{\phi}{g_{z1}})$	SD3
$Z^*_1 + Z^*_2$	=	$\frac{\gamma}{m_z}S^*_{R_p} - m_p(1-\phi)(\frac{1}{g_{z1}} + \frac{1}{g_{z2}})$	SD4
Insight SDI:		P_1 and P_2 co-exist if $\phi < \frac{g_{z2}}{g_{z1}} < \frac{1}{\phi}$	
Insight SDII:		$P_1 < P_2$ if $g_{z1} > g_{z2}$	
Mechanism E		Different limiting resource (Follows et al., 2018; Dutkiewicz et al., 2020; Ward et al., 2013; Dutkiewicz et al., 2014)	
R^*_{Xp1}	=	$\frac{\kappa_{pX1}m_p}{\mu^{max}_{pj=1}-m_p}$	SE1
R^*_{Yp2}	=	$\frac{\kappa_{pY2}m_p}{\mu^{max}_{p2}-m_p}$	SE2
P^*_1	=	$\frac{1}{m_p}S^*_X$	E3
P^*_2	=	$\frac{1}{\Upsilon_{XY2}}(S^*_Y - \Upsilon_{XY1}S^*_X)$	SE4
Insight SEI:		P_1 and P_2 co-exist if $\frac{S^*_Y}{S^*_X} > \Upsilon_{XY1}$	

Supplemental Table S3: Steady state solutions for the mechanisms laid out in Supplemental Table S2 and Figure 3, and insights into when plankton co-exist. These solutions are for when all plankton in the frameworks co-exist, as shown in Figure 3 for sectors iv (Mechanism A), iii (Mechanism B), vi (Mechanism C), iv (Mechanism D), and i (Mechanism E).

Experiment	**Mechanism targeted**	**Difference to Default**	**References**
EXP-0		default	
EXP-A	Size-specific grazing (Mechanism A)	single generalist grazer	Dutkiewicz et al. (2020)
EXP-B	Third Trophic Level (Mechanism B)	no carnivory	
EXP-C	Shared predation with bacteria (Mechanism C)	no explicit bacteria	Follett et al. (2021)
EXP-D	Shared predation with other size classes of phytoplankton (Mechanism D)	**1.** no cross-size grazing ($\phi = 0$); **2.** higher cross-grazing for Syn/Pro ($\phi = 0.6$)	
EXP-Ea	Ratio of supply of different nutrients (Mechanism E)	**1** half aeolian iron supply; **2** double aeolian iron supply	Dutkiewicz et al. (2012, 2014)
EXP-Eb	Silica requirement for diatoms	**1** half diatom requirement for Si; **2** double diatom requirement for Si	

Supplemental Table S4: Numerical model sensitivity experiments use to test each of Mechanisms A to E (Figs. 3, 6b) as well as additional experiments to test role of silicic acid requirements of diatoms. We include references for studies with similar experiments.

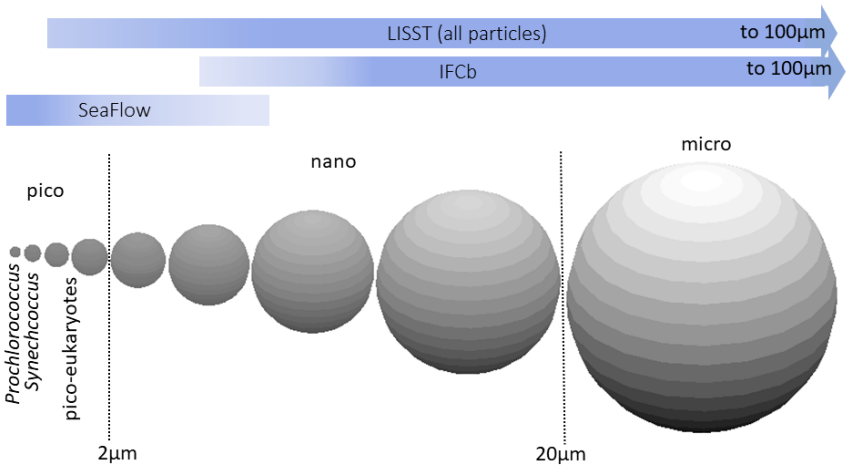

Supplemental Figure S1: Schematic showing relative size of different phytoplankton types in terms of their equivalent spherical diameter (ESD): *Prochlorococcus*; *Synechococcus*; pico-eukaryote; as well as nano-size classed cells such as diazotroph UCYN-A (usually $<3\mu$m) and diatoms ($>3\mu$m). LISST and IFCB capture cells up to $\sim$ 100 μm, for clarity in this schematic we only show to 22μm. Most cells are not perfect spheres, and as such the equivalent spherical diameter is used to compare different size classes. At the top of figure are depiction of the size range covered by each optical instrument used in the SCOPE-Gradients cruises (SeaFlow, IFCB, LISST) with shading showing relative level of uncertainty (fainter for more uncertain).

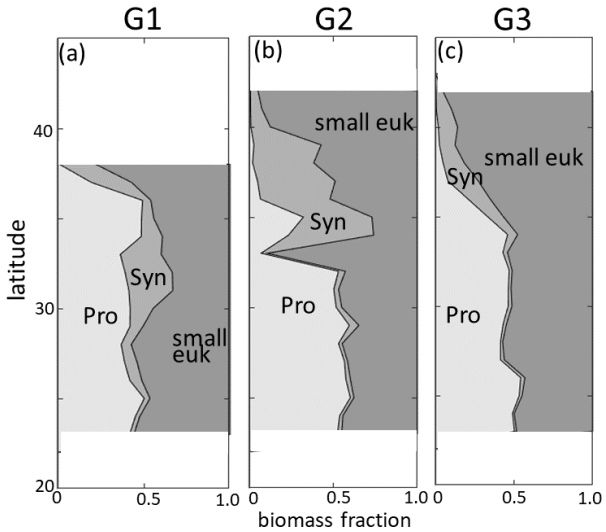

Supplemental Figure S2: Flow Cytometry (Seaflow) data along SCOPE-Gradients transects showing fraction of total $\sim$ 0.5 - 3μm phytoplankton biomass in each of *Prochlorococcus* (lightest shade), *Synechococcus* (medium shade) and small-eukaryotes (1.2-$\sim$3μm, darkest shade), (a) G1, (b) G2, (c) G3.

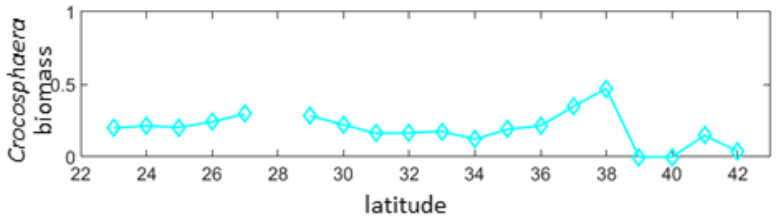

Supplemental Figure S3: The diazotroph *Crocosphaera* biomass (mg C m^{-3}) as estimated from SeaFlow data average into 1^o latitude bins. This species was not detected by SeaFlow during G1 and G2, but was detected through *nifH* gene copies (Gradoville et al., 2020) in all three cruises.

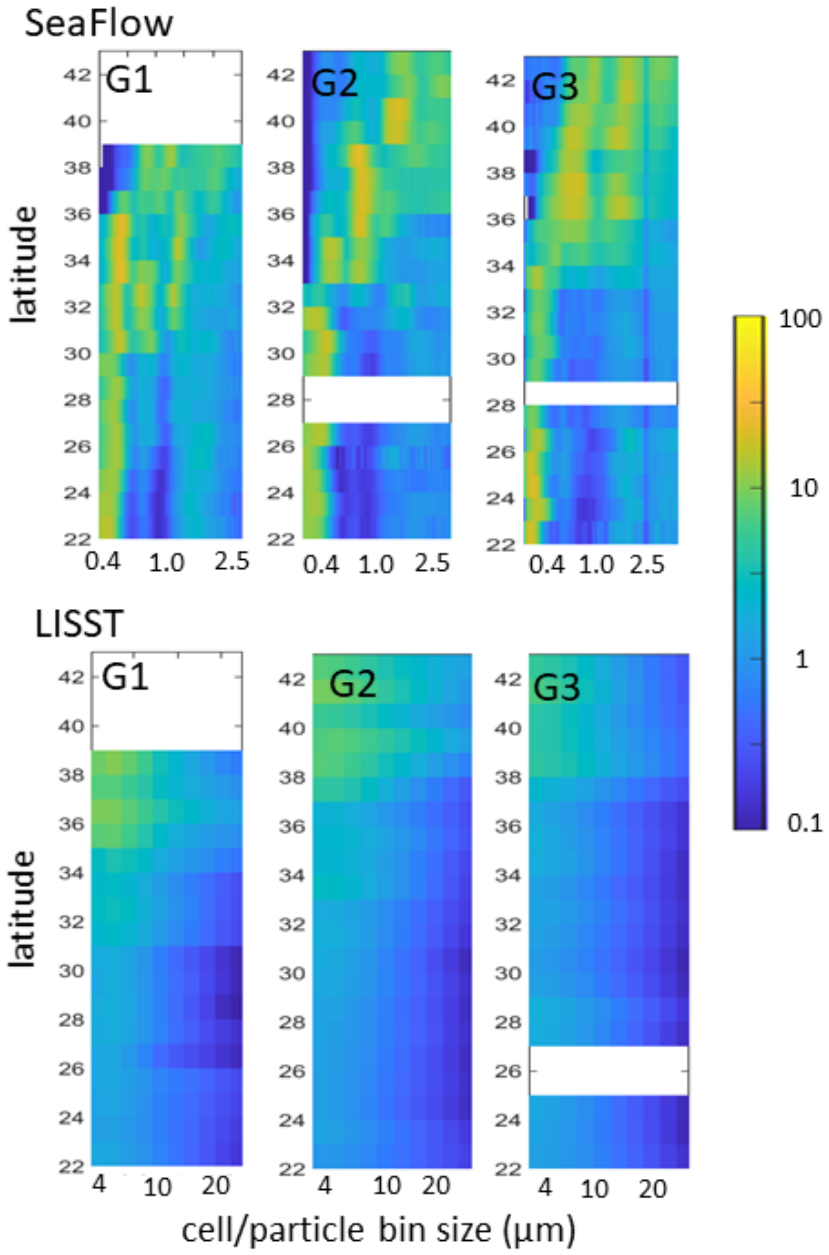

Supplemental Figure S4: Normalized carbon concentration (mg C m^{-3} μm^{-1}) for small phytoplankton (top panel), and for particulate organic carbon (including phytoplankton, other plankton and detrital matter, bottom panel) in size bins for each cruise G1, G2, G3. Data is averaged over 1^o latitude bins. Top panels come from SeaFlow, and bottom panel from LISST. Each size bin is a different width, and as such we normalize each value by the size bin width so that the values are comparable. The pattern of more biomass in larger size classes transecting further north is clearly shown. Similar plots have been shown in Juranek et al. (2020).

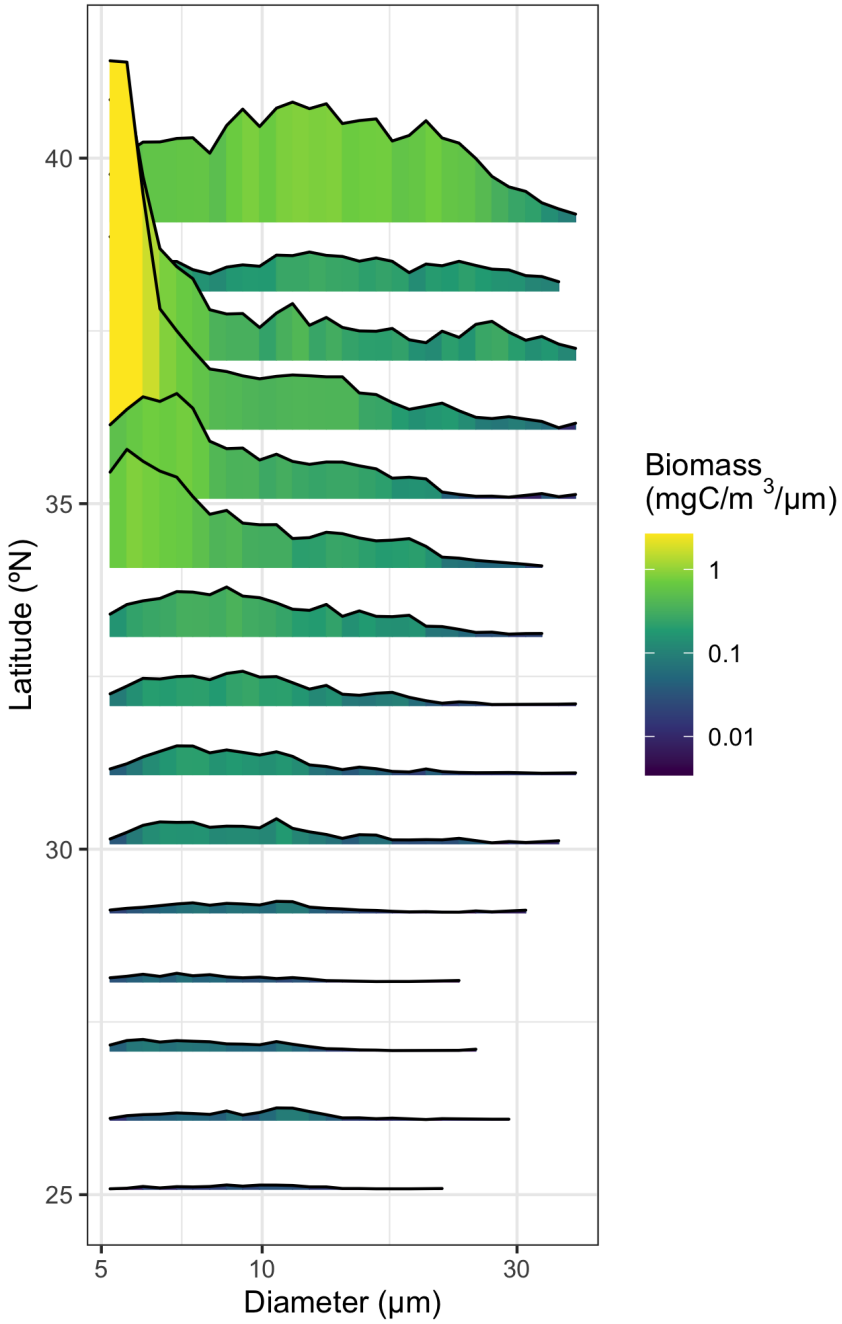

Supplemental Figure S5: Normalized carbon biomass (mg C m^{-3} μm^{-1}) size distribution for phytoplankton for G2 from IFCB in 1^o latitude averaged bins. Each size bin is a different width, and as such we normalize each value by the size bin width so that the values are comparable. The pattern of more biomass in larger size classes transecting further north is clearly shown. IFCB data was not available for G1 and has not be analysed for G3.

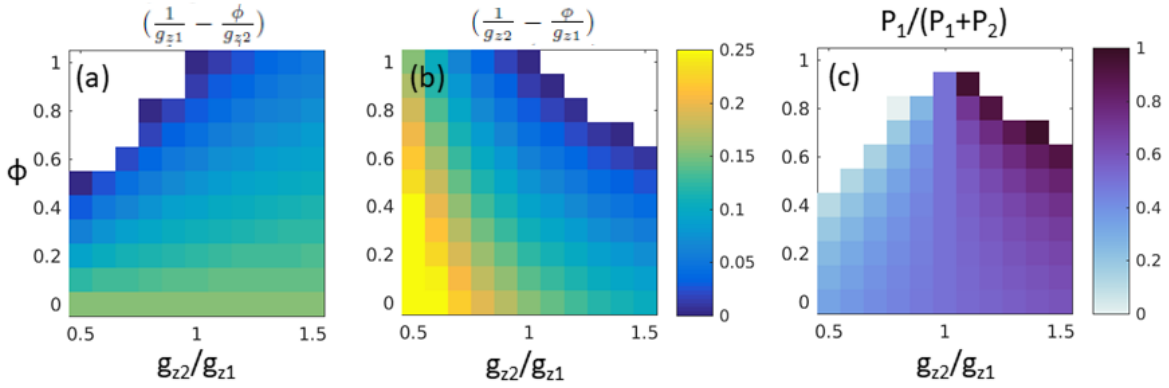

Supplemental Figure S6: Exploring cross-grazing theoretical framework (Mechanism D). Relative magnitude of the biomass represented by the parts of equations from Supplemental Table S3 (Eqs. SD2, SD3) that differ ($\frac{1}{g_{zj}} - \frac{\phi}{g_{zk}}$) for (a) P_1 and (b) P_2. Axes are the strength of the cross-grazing for the less preferred prey ($\phi = 1$ indicates both prey are equally preferred, $\phi = 0$ indicates that the less preferred prey is not targeted) and the ratio of the grazing rates (i.e. 1 indicates that $g_{z1} = g_{z2}$). Values of g_{z1} are taken from the numerical model for the third smallest zooplankton (6.5 d^{-1}). (c) The fraction of P_1 of the combined biomass ($P_1 + P_2$). P_1 represents a lower fraction of the biomass when g_2 is lower than g_1 and ϕ is high. White areas indicate where one or the other of the phytoplankton are completely excluded.

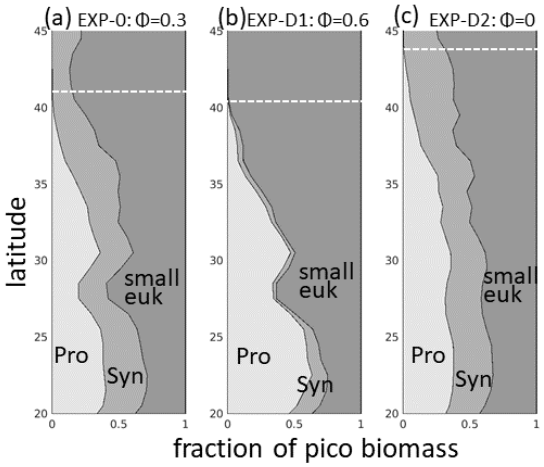

Supplemental Figure S7: Sensitivity experiments to explore importance of shared grazing with different size classes: Latitudinal (along 158°W) distribution of modeled annual mean fraction of picophytoplankton biomass(<3 μm) in each of *Prochloroccocus* (lightest shading), *Synechococcus* (medium shading), and small eukryotes (darkest shading) for (a) EXP-A(default, with ϕ=0.3); (b) EXP-D1 (higher cross-size class grazing, $\phi = 0.6$); (c) EXP-D2 (no cross-size class grazing, $\phi = 0$). ϕ here is the zooplankton preference for grazing on less preferred plankton types. Horizontal dashed lines indicate where *Prochlorococcus* biomass vanishes. Difference maps relative to EXP-0 are shown in Supplemental Figure S9.

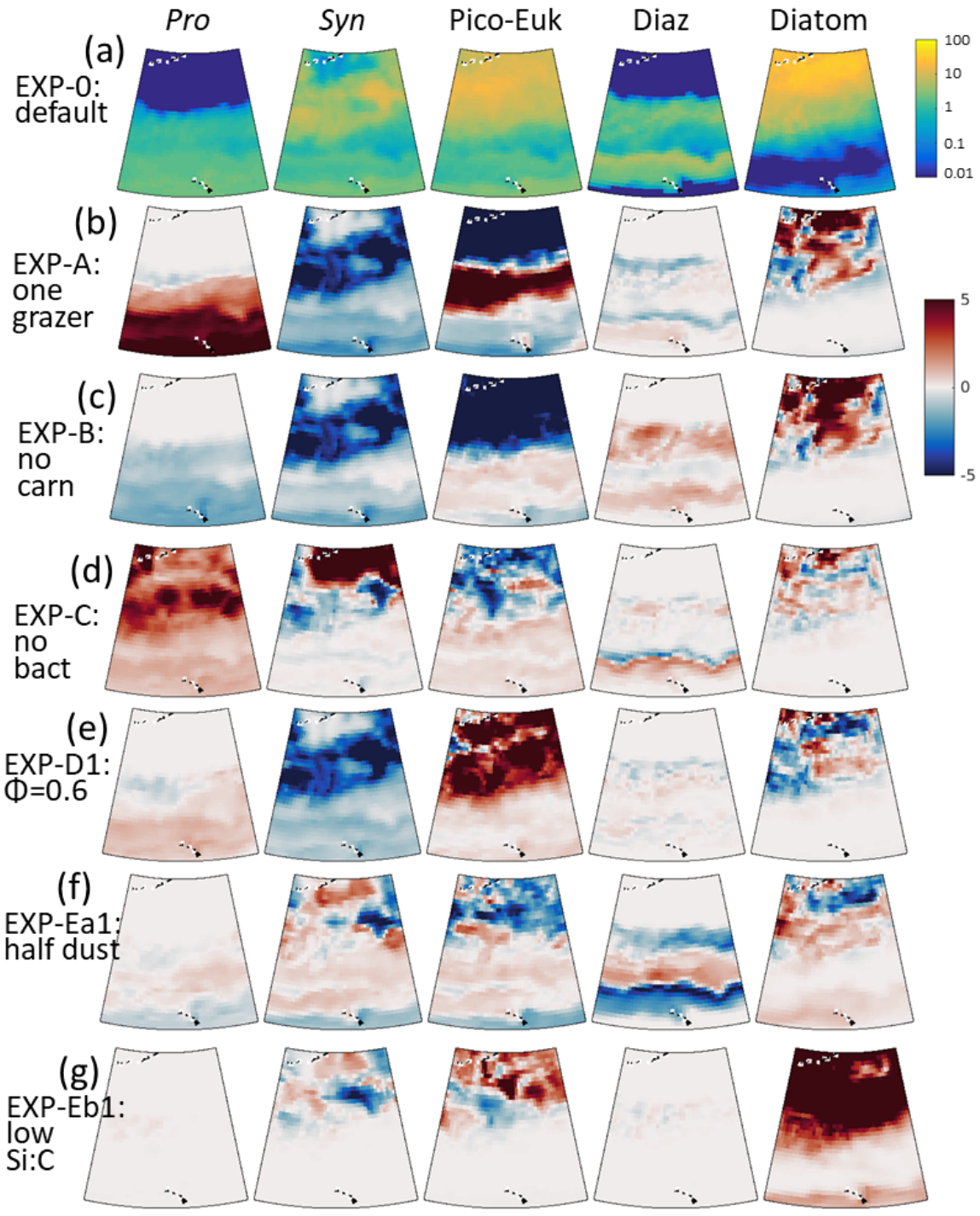

Supplemental Figure S8: (a) Modeled annual mean biomass (0-10 m) of *Prochloroccocus*, *Synechococcus*, pico-eukaryotes, diazotrophs and diatoms (mg C m^{-3}) for EXP-0 (the default). The remaining rows show the difference (mg C m^{-3}) between experiments and the default (positive indicates that EXP-0 has higher values than the sensitivity experiments): (b) EXP-A (single generalist grazer); (c) EXP-B (no carnivory); (d) EXP-C (no explicit bacteria); (e) EXP-D1 (higher cross-size class grazing); (f) EXP-Ea1 (low aeolian iron deposition); (g) EXP-Eb1 (lower requirements of silica in diatoms). Here we show results only for the North East Pacific, but the simulation was global.

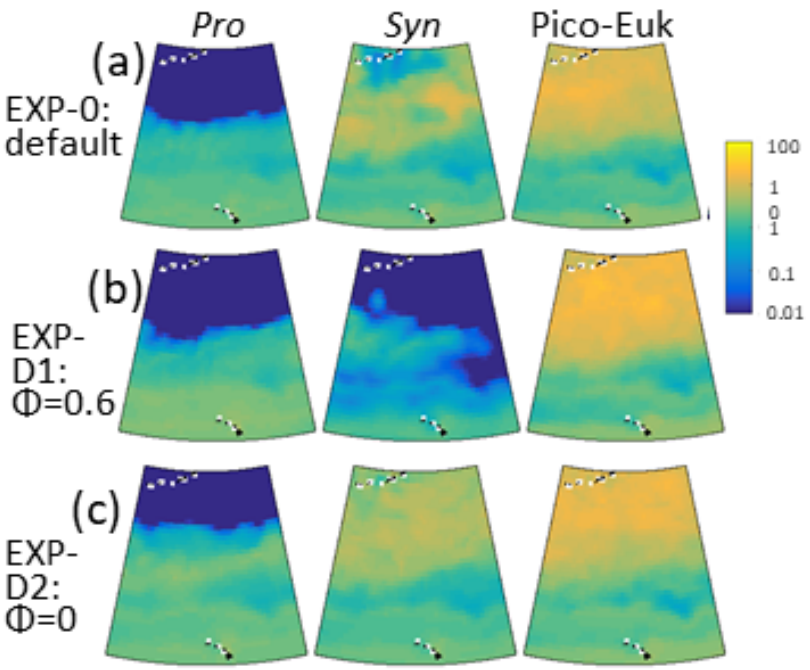

Supplemental Figure S9: Modeled annual mean biomass (0-10 m) of *Prochloroccocus*, *Synechococcus*, pico-eukaryotes (mg C m^{-3}) for (a) EXP-0 (default, $\phi = 0.3$); (b) EXP-D1 (higher cross-size class grazing, $\phi = 0.6$); (c) EXP-D2 (no cross size class grazing, $\phi = 0$).

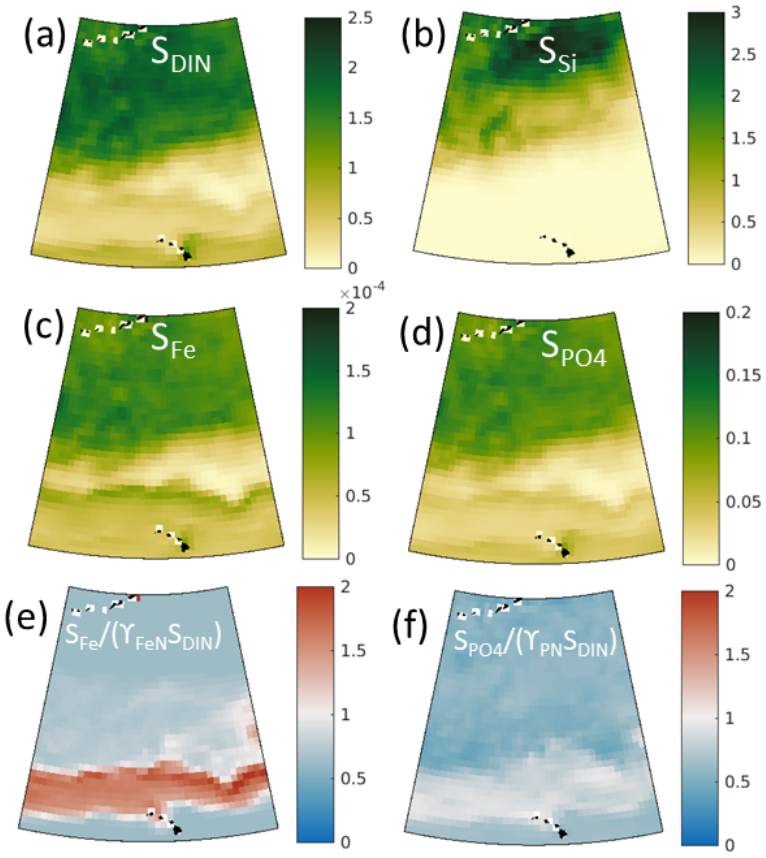

Supplemental Figure S10: Annual average modelled inorganic resources supply rate into the upper 50 m of the ocean (mol m^{-2} y^{-1}) (a) Dissolved Inorganic Nitrogen (DIN), S_{DIN} (b) Silicic Acid, S_{Si}, (c) dissolved iron, S_{Fe}, (d) phosphate, S_{PO4}, (e) ratio of Fe to DIN supply rate relative to non-diazotrophs needs, $S_{Fe}/(\gamma_{FeN} S_{DIN})$, (f) ratio of PO_4 to DIN supply rate relative to non-diazotrophs needs, $S_{PO4}/(\gamma_{PN} S_{DIN})$. Diazotrophs co-exist with non-diazotrophs when Fe and PO_4 are supplied in excess of the non-diazotrophs needs (i.e. when regions where both (e) and (f) are greater than ratio of 1). Note that region of excess iron and phosphate supply varies, leading to the expansion and contraction of the diazotroph range over the course of the year (Supplemental Fig. S13d). Here we show results only for the North East Pacific, but the simulation was global.

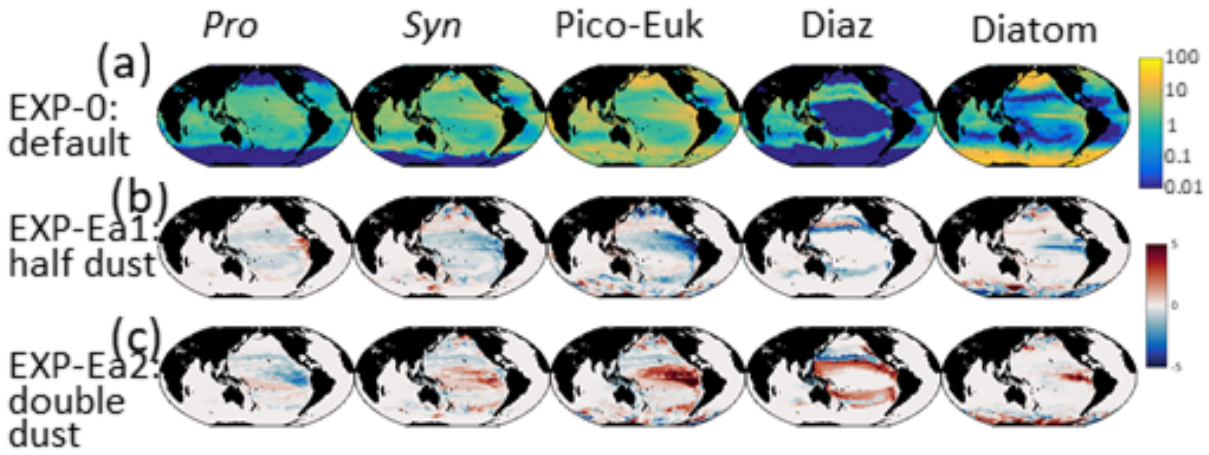

Supplemental Figure S11: (a) Modeled annual mean biomass (0-10 m) of *Prochloroccocus*, *Synechococcus*, pico-eukaryotes, diazotrophs and diatoms (mg C m^{-3}) for EXP-0 (the default); and the difference (mg C m^{-3}) between experiments and the default (positive indicates that EXP-0 has higher values than the sensitivity experiments) for: (b) EXP-Ea1 (lower aeolian iron deposition); (c) EXP-Ea2 (higher aeolian iron deposition). Aeolian iron dust fluxes where half those in EXP-0 for EXP-Ea1 and double for EXP-Ea2. Global maps are shown to indicate the the larger scale impacts: In EXP-Ea1, lower iron supply in iron limited regions such as the equatorial Pacific leads to lower diatoms, which in turn allows excess silicic acid to propogate into the southern portion of our region of interest (see Fig. 5f) and allow diatoms to survive there. The opposite effect occurs in EXP-Ea2 where higher diatom growth along the equator reduces the supply of silicic acid into our region, reducing diatoms population there.

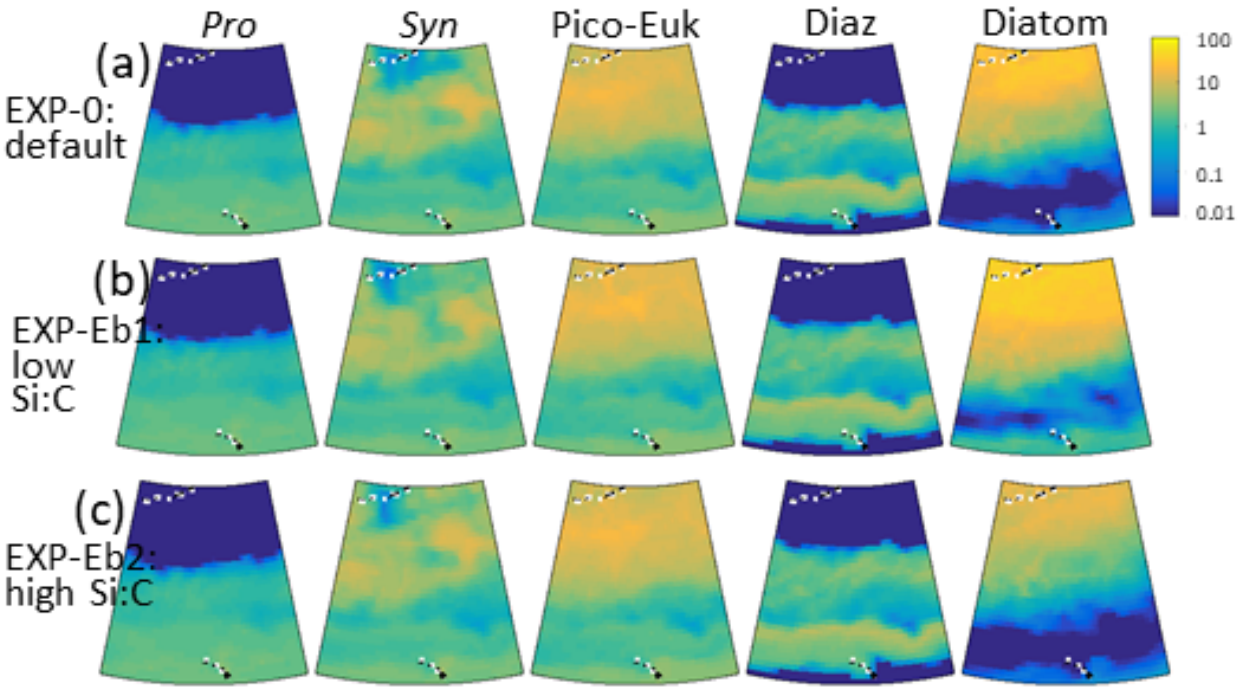

Supplemental Figure S12: Modeled annual mean biomass (0-10 m) of *Prochloroccocus*, *Synechococcus*, pico-eukaryotes, diazotrophs and diatoms (mg C m^{-3}) for: (a) EXP-0 (the default); (b) EXP-Eb1 (lower silica needs for diatoms); (c) EXP-Eb2 (higher silica needs for diatoms). Si:C stoichometery for EXP-Eb1 were half what they were in EXP-0, and double in EXP-Eb2.

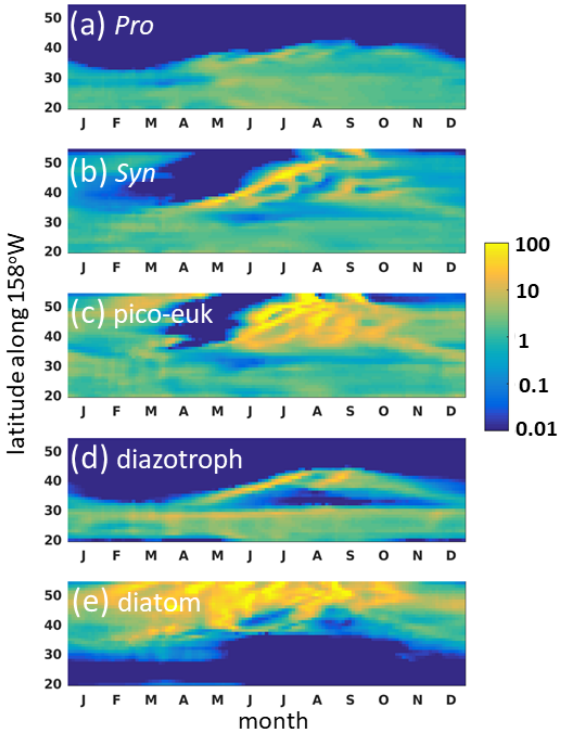

Supplemental Figure S13: : Modeled timeseries for annual cycling of (surface, 0-10 m) biomass (mg C m^{-3}) along longitude 158^{o}W of (a) *Prochlorococcus*, (b) *Synechococcus*, (c) pico-eukaryotes, (d) diazotrophs and (e) diatoms for default experiments (EXP-0).